

The $\Sigma 13$ ($10\bar{1}4$) twin in $\alpha\text{-Al}_2\text{O}_3$: A model for a general grain boundary

Stefano Fabris and Christian Elsässer

Max-Planck-Institut für Metallforschung, Seestrasse 92, D-70174 Stuttgart, Germany

(November 2, 2018)

The atomistic structure and energetics of the $\Sigma 13$ ($10\bar{1}4$) symmetrical tilt grain boundary in $\alpha\text{-Al}_2\text{O}_3$ are studied by first-principles calculations based on the local-density-functional theory with a mixed-basis pseudopotential method. Three configurations, stable with respect to intergranular cleavage, are identified: one Al-terminated glide-mirror twin boundary, and two O-terminated twin boundaries, with glide-mirror and two-fold screw-rotation symmetries, respectively. Their relative energetics as a function of axial grain separation are described, and the local electronic structure and bonding are analysed. The Al-terminated variant is predicted to be the most stable one, confirming previous empirical calculations, but in contrast with high-resolution transmission electron microscopy observations on high-purity diffusion-bonded bicrystals, which resulted in an O-terminated structure. An explanation of this discrepancy is proposed, based on the different relative energetics of the internal interfaces with respect to the free surfaces.

61.72.Mm,61.72.Bb,73.20.At,71.15.Ap

I. INTRODUCTION

Alumina ($\alpha\text{-Al}_2\text{O}_3$) is widely used in polycrystalline forms. Small amount of various dopant elements (typically Mg, Ca, Si, and Ti) are added in the synthesis of alumina polycrystals, either to promote sintering, or to obtain empirically optimized microstructures (grain size and shape distributions) for technological applications.¹ Due to the very small solubility limit in bulk for many impurities (typical values are 10 ppm for yttrium,² 30 ppm for calcium,³ 300 ppm for silicon³), they segregate to grain boundaries (GB).⁴ The segregation of different species at grain boundaries drastically modifies the properties of alumina, in either beneficial or undesired manner. For instance, the isovalent cations Y and La reduce the mechanical creep rate of polycrystalline alumina by 2–3 orders of magnitude,^{5,6} Si and Ca promote exaggerated grain growth,^{3,7} and Ca may affect the fracture properties, decreasing the strength and toughness of the material.^{8,9} From a fundamental aspect of science, a key issue in alumina systems is therefore the microscopic understanding of internal interfaces and of grain-boundary impurity segregation.

This study is part of an extended project that aims to correlate the macroscopic structural proper-

ties of alumina to its microscopic structure. The project combines empirical atomistic modelling and first-principles electronic-structure theory with experimental high-resolution transmission electron microscopy (HRTEM) and with analytical electron microscopy (AEM), in particular spatially resolved electron energy-loss near-edge spectroscopy (ELNES). In this framework a set of four grain boundaries were selected for a fundamental theoretical study of atomistic and electronic structures: the basal $\Sigma 3$ (0001), the rhombohedral $\Sigma 7$ ($10\bar{1}2$), the $\Sigma 13$ ($10\bar{1}4$), and the prismatic $\Sigma 3$ ($10\bar{1}0$) twin boundaries. This set provides a couple of mutually orthogonal twin interfaces, basal and prismatic, and a couple of nearly orthogonal ones, the $\Sigma 7$ and the $\Sigma 13$.

The basal and rhombohedral twin interfaces have recently been studied in detail by means of ab-initio local-density-functional theory (LDFT) and empirical shell-model calculations.^{10–12} The theoretical analysis of the interface structure for the rhombohedral twin has been confirmed quantitatively by both HRTEM and ELNES experiments,¹³ validating the accuracy and predictive power of the theoretical approach, which is employed as well in the present work dealing with the $\Sigma 13$ twin interface. Results for the prismatic twin interface will be reported separately¹⁴.

Several studies indicated that the segregation of impurities like Ca or Y to GB is more favourable for general, disordered interfaces than for special ones with high structural order and energetic stability.^{15,16} This is commonly rationalized by the large mismatch in ionic radii between the segregated species ($r_i=0.94$ Å for Ca^{2+} and $r_i=0.88$ Å for Y^{3+} , Ref. 17) and the host-lattice element Al^{3+} ($r_i=0.45$ Å, Ref. 17). General boundaries provide more excess volume at the interface, and the oversized Ca and Y cations fit more easily here than at special GB, where the interfacial atomic environment is highly ordered and compact. As an example, the impurity level in the nearly bulk-like rhombohedral and prismatic twin boundaries is below the detection limit of 0.3 atoms/nm².¹⁸ There are indications that the basal plane may have an atomic environment which is slightly more favourable to segregation.^{18–20} Compelling experimental evidence for segregation to a twin boundary was observed for the case of the $\Sigma 13$ ($10\bar{1}4$) twin boundary.²¹

Among the four selected GB, the interfacial structure of the $\Sigma 13$ boundary is the most different from the bulk atomic environment of $\alpha\text{-Al}_2\text{O}_3$. Hence it is anticipated to have a rather high interface energy, and it seems to be best suited and most promising to address the issue of segregation of cation impurities to GB. Its interfa-

cial structure appears sufficiently disordered and open to accept likely segregated impurities, thus being representative for the atomic environment in a general GB. At the same time it is sufficiently ordered, with short lateral periodicity along the interface, that it can be described with some tens of atoms. Hence it is accessible via first-principles LDFT calculations. In the present work we consider the $\Sigma 13$ twin boundary as a representative case to study the effect of segregation on the mechanical and electronic properties of alumina interfaces. We describe the properties of the pure $\Sigma 13$ twin interface in this paper, and the modifications induced by the segregated atoms in a forthcoming one.

Theoretical investigations preceding ours of the same $\Sigma 13$ twin have been undertaken by Finnis and coworkers. To our best knowledge, results have been published only for empirical shell-model calculations,^{22–24} but not for ab-initio LDFT calculations.²⁵

This paper is arranged as follows: A short review of previous studies on the $\Sigma 13$ twin boundary is presented in Section II. A brief description of the employed computational methods is given in Sec. III. The results of our investigation, namely the mechanical stability, the relative energetics, and the electronic structure of different metastable structural variants for the $\Sigma 13$ interface are reported and discussed in Sec. IV. Final remarks and a summary are made in Section V.

II. PREVIOUS STUDIES ON THE $\Sigma 13$ TWIN BOUNDARY

Figure 1 shows the crystal structure of $\alpha\text{-Al}_2\text{O}_3$ (corundum, space group $R\bar{3}c$), projected on the $(\bar{1}2\bar{1}0)$ plane: light and dark circles represent oxygen and aluminium ions, respectively. The structure can be described as a nearly ideally close packed hexagonal oxygen sublattice with $2/3$ of the available octahedral interstices filled by Al cations. The remaining octahedral sites are empty, and the partial filling results in small internal atomic displacements in both sublattices, which are visible in Figure 1. The $\Sigma 13$ $(10\bar{1}4)$ twin interface is formed by two grains with a relative misorientation given by the planes $(10\bar{1}4) \parallel (10\bar{1}4)$ and the directions $[\bar{1}2\bar{1}0] \parallel [\bar{1}2\bar{1}0]$.

High-resolution transmission electron micrographs of high-purity diffusion-bonded bicrystals containing this interface²² revealed two distinct boundary structures. The images differed by the sequence of intensity maxima across the boundary: one showed a continuous (C) and the other a broken (B) pattern of spots across the boundary. The C interface was found in the bicrystal bonded without further treatment, besides sufficient cleaning of the free surfaces, while the B and C interfaces coexisted when a metallic Al layer was deposited on the free surfaces after the cleaning and before the diffusion-bonding process.

Atomistic modelling based on empirical classical potentials^{22,23} also identified two boundary structures, in

which the two grains were either Al or O terminated. They predicted the former to be more stable than the latter. The calculated interface energies for the two relaxed boundaries were 1.7 J m^{-2} (Al-terminated) and 2.1 J m^{-2} (O-terminated), respectively.

The details of these interface structures were not directly accessible from the HRTEM images alone. The combination of atomistic modelling and image simulations allowed an assignment of the B and C patterns to cation and anion terminated interfaces, respectively.²² The corresponding terminating planes in the perfect corundum structure of Figure 1 are marked by the dashed lines labelled B and C.

Höche and Rühle studied the segregation of calcium to the $\Sigma 13$ boundary and the resulting structural modifications induced on the B and C structures.²¹ A layer of metallic calcium, 3 nm thick, was deposited on one of the $(10\bar{1}4)$ free surfaces after cleaning and before diffusion-bonding the bicrystal. After the bonding procedure, $2.4 \pm 0.9 \text{ Ca ions per nm}^2$ were detected at the interface,²⁶ therefore proving that Ca segregates to this grain boundary. Again, as in the Al-doped case, two distinct structures coexisted: one variant showed little differences to the C structure. The other was qualitatively similar to the B structure but with significant quantitative differences. In this case the comparison of the HRTEM with theoretical calculations was not possible because atomistic calculations of cation segregation at alumina grain boundaries were not available.

Such results raise fundamental questions on the formation mechanism and kinetics of interfaces. In the specific case of the $\Sigma 13$ twin boundary, the most common structure observed in diffusion-bonded bicrystals (O-terminated) is apparently not the one with the minimum energy predicted by the theoretical calculations (Al-terminated). Hence, is the $\Sigma 13$ twin boundary a case in which empirical atomistic model potentials reach their limit of predictive power? This concern is assessed by employing the non-empirical LDFT approach for the theoretical investigation. Or is the $\Sigma 13$ twin boundary rather a case where diffusion-bonding of the lowest-energy surfaces does not immediately result in the lowest-energy interface? This possibility is investigated by mapping theoretically the relative energetics along configuration paths for both bonding the most stable surfaces together and pulling the most stable interface apart. The paper provides a precise description of the interfacial atomic environment and electronic structure of the $\Sigma 13$ twin boundary, and it proposes an explanation of the difference between experimental HRTEM observations and theoretical predictions.

III. COMPUTATIONAL METHODS

In this work we used the same computational approach as previously for the rhombohedral twin boundary,¹⁰ the

basal twin boundary,¹¹ and basal-plane stacking faults,²⁷ namely atomistic modelling with empirical interatomic potentials and ab-initio LDFT calculations.

The empirical potentials which were used in the atomistic modelling of α -Al₂O₃, were taken from Lewis and Catlow²⁸. They incorporate the long-range Coulomb interaction between all Al cations and O anions, the short-range ion-overlap repulsion, the weak Van-der-Waals attraction between the anions, and a shell-model dipole polarizability of the anions. The cations were treated as non polarizable and mutually interacting via Coulomb repulsion only. The advantage of the empirical potentials with respect to LDFT is their superior computational simplicity, the disadvantage is their limited reliability for predictions of material-specific properties. The comparison of the two approaches^{11,27} for basal-plane twin-boundary structures and stacking faults in α -Al₂O₃ showed that the empirical potentials can provide quantitatively not very accurate interface energies, but qualitatively correct energy hyperfaces in structural parameter spaces. Atomistic arrangements in metastable structures obtained by both approaches were found to be very similar, making the empirical potentials very useful for identifying relevant initial grain-boundary configurations, that can then be structurally optimized with the LDFT.

The LDFT calculations were made by means of the mixed-basis pseudopotential technique for the computation of electronic structures, total energies, and forces in crystalline materials. The interfaces were described by supercells with periodic boundary conditions. The computational details, namely the norm-conserving ionic pseudopotentials for Al and O, the mixed basis for the representation of the valence-band and conduction-band Bloch states in α -Al₂O₃, the discrete Brillouin-zone integration meshes etc. were the same as, or equivalent to the ones used in our previous investigations.¹⁰⁻¹² For the optimization of the interface structures, excess expansions of the interfaces were obtained via total-energy minimization with respect to the axial supercell length. Simultaneously, to account for lateral grain translations as well, all atomic positions in the supercells were statically relaxed according to the acting forces.

Numerous published studies of various materials' structures and properties from the Stuttgart groups and others involved in developments of the mixed-basis pseudopotential approach²⁹⁻³³ have documented the accuracy, efficiency and predictive power of this density-functional technique. Specifically for α -Al₂O₃, bulk structural parameters of corundum were compared to results from other LDFT methods and from experiment in Table 1 of Ref. 10, and the predictive power of the method for grain-boundary structures was demonstrated in Ref. 27.

The unit cells used to model the Σ 13 twin interface were constructed by cutting the corundum structure of α -Al₂O₃ with a (10 $\bar{1}$ 4) plane and rotating one half of the crystal with respect to the other by 180°, around the interface-plane normal vector $\mathbf{n}_{\text{GB}}=[50\bar{5}4]$ (symmetrical

twist). Note that in hexagonal coordinates the [50 $\bar{5}$ 4] direction is orthogonal to the (10 $\bar{1}$ 4) plane. The rotation axis \mathbf{n}_{GB} contains a center of inversion symmetry for the original corundum structure, therefore the resulting bicrystal is mirror-symmetric.

This procedure was applied to the cutting planes B and C marked by the dashed lines in Figure 1, leading to the starting configurations for two stoichiometric variants of the grain boundary. The computational cell was then obtained by cutting a slab centered on the grain boundary, and repeating it with periodic boundary conditions. The slab-edges identifying the shape of the orthorhombic supercell are $\mathbf{e}_1 \parallel [20\bar{2}1]$, $\mathbf{e}_2 \parallel [1\bar{2}10]$, and $\mathbf{e}_3 \parallel [50\bar{5}4]$.

The size of the slab along \mathbf{e}_3 was selected so that it contained two equivalent interfaces, one in the middle, already described, and one at the edges, arising as a consequence of the periodic boundary conditions. A careful choice of the supercell size along \mathbf{e}_3 was necessary in order to minimize the spurious interaction between the two equivalent boundaries. The convergence of the results against the interface-interface distance was checked by considering 3 supercells, with 10, 15, and 20 atomic layers between the boundaries, corresponding to 40-, 60-, and 80-atom supercells. The results for the small cell were already converged in the case of the cation terminated interface while the 60-atom cell was necessary for the anion terminated one. We will further discuss this issue in the following.

IV. RESULTS AND DISCUSSION

A. Lateral translation state

The twin-boundary equilibrium configurations were found with increasing degrees of accuracy, by combining empirical atomistic and first-principles calculations. Previous studies showed that the empirical shell-model potential provides the correct qualitative description of the energetics and structure of twin boundaries.^{10,11} This makes the shell-model suitable for a first exploration of possible metastable configurations.

Using this model and the computer program GULP,³⁴ we calculated the bicrystal energetics as a function of the relative displacement of one grain with respect to the other along the interface plane. The relative displacement is defined by the lateral translation vector $T_1\mathbf{e}_1 + T_2\mathbf{e}_2$, where T_1 and T_2 are fractional coordinates with respect to the lattice vectors \mathbf{e}_1 and \mathbf{e}_2 . The interfacial symmetry confines the non-equivalent part of the energy surface to a quarter of the lateral repeat unit cell, limited by the interval between 0 and 0.5 for both T_1 and T_2 .

The starting boundary structures, corresponding to $(T_1, T_2)=(0,0)$, were the mirror-symmetric interfaces obtained as described in the previous section. It is clear that these structures are highly unstable because equal

charges on opposite sides of the boundary face each other at very close distances. This is the reason why atomic relaxation was not considered in this preliminary analysis of the translation state. The shell-model potentials are not suitable to describe such highly non-equilibrium structures and would predict large unrealistic relaxations. Only the metastable structures identified with the static shell-model calculations were relaxed subsequently, according to both empirical shell-model and first-principles forces on the individual atoms.

1. Cation terminated interface

The cation terminated interface was obtained by cutting the corundum structure along line B in Figure 1 and building the supercell as described above. The energy surface, governing the inter-granular lateral translation state, as a function of (T_1, T_2) is shown in Figure 2.

The starting configuration $(T_1, T_2)=(0,0)$ is expected to be unstable because it faces equal charges very close to each other, on opposite sides of the boundary. The shell-model predicts the highest energy for this configuration. The total energy is minimized by the lateral translation state $(T_1, T_2)=(0.25,0.5)$, resulting in an Al terminated structure with glide-mirror symmetry with respect to $(10\bar{1}4)$. This configuration, which we will indicate as G(Al), maximizes the inter-granular distance between equal charges and minimizes that one between opposite charges. Alternating triplets of oxygen atoms at the interface $(O(1)-O(2)-O(3))$ and $(O(1)^*-O(2)^*-O(3)^*)$ in Figure 3) characterize this boundary.

The structure was then relaxed according to the forces from the shell model as well as from the LDFT. The results were qualitatively equivalent: the stable translation state was the same, and internal relaxations involved only ions in the neighbourhood of the interface, namely the atomic layers from $O(2)$ to $O(2)^*$. The LDFT relaxed structure is shown in Figure 3. It has the same features as the cation-terminated interface identified in Ref. 22: an HRTEM setting for this interface showing the holes as intensity maxima would produce a broken pattern of white spots across the boundary.

In order to check the adequacy of the supercell size perpendicular to the interface, the relaxation procedure was made for 40- and 60-atom supercells. The small difference between the interface energies ($< 4\%$) of the two supercells showed that convergence was already achieved with the small cell.

2. Anion terminated interfaces

A similar procedure was carried out for the anion terminated interface, which was obtained by cutting the single crystal along line C in Figure 1. Note that in this case the interface plane coincides with an atomic oxygen layer.

The total energy as a function of the lateral translation state (T_1, T_2) is shown in Figure 4 and predicts three metastable configurations.

The structure with the lowest energy has a translation state of $(T_1, T_2)=(0.25,0)$, and corresponds to the Al-terminated boundary already described above. This is an important feature of this boundary: the same Al-terminated interface may be obtained either by cutting the single crystal along B (Figure 1), rotating one grain around \mathbf{n}_{GB} by 180° and imposing the lateral translation state $(T_1, T_2)=(0.25,0.5)$, or by cutting along C, rotating one grain around \mathbf{n}_{GB} by 180° and imposing the lateral translation state $(T_1, T_2)=(0.25,0)$. In the latter case the initial boundary was on an O layer, but the glide-mirror symmetry operation reconstructs a bulk-like environment near the atomic layer at C, and shifts the boundary by two atomic layers from O termination (C) to Al termination (B).

The structure with the second lowest energy is defined by the lateral translation state $(T_1, T_2)=(0.5,0.5)$. It has an oxygen layer on the boundary plane, and the grains are related by a glide-mirror symmetry with respect to $(10\bar{1}4)$. We will denote it by G(O). Similarly to the Al-terminated case, both the LDFT and shell-model atomic relaxations predict the metastability of this translation state: the atomic relaxation involves mainly the first three interfacial layers. The relaxed supercell is shown in Figure 5. Note the characteristic ‘V’ shape formed by the interfacial O atoms $(O(1)-O(0)-O(1)^*)$ in Figure 5). A HRTEM micrograph of this structure showing the holes as white spots would produce a continuous pattern across the boundary.

Finally, the metastable structure with the highest energy is obtained by the translation state $(T_1, T_2)=(0,0.5)$, leading to an O-terminated configuration with a twofold screw-rotation symmetry around $[20\bar{2}\bar{1}]$. It is denoted as S(O). The relaxed supercell is shown in Figure 6. Both the LDFT and shell-model atomic relaxations show that this translation state is not stable. The atomic forces drive the bicrystal towards $(T_1, T_2)=(0.12,0.5)$. This is a new metastable interface structure that was not noticed in the previous studies of this GB. Holes would produce a broken pattern of spots, intermediate between the G(O) and G(Al) ones.

Also for G(O), the adequacy of the axial supercell size was checked by comparing the relaxation patterns obtained with 40-, 60-, and 80-atom supercells. The LDFT relaxation of the 40-atom cell involved all the atoms hence leaving virtually no bulk-like volume remote from the boundary, while the shell-model relaxation eliminated the boundaries, reconstructing a single-crystal. This procedure indicated that the 40-atom cell is too small for the O-terminated interfaces. The LDFT and shell-model relaxations for the 60-atom supercell proceeded leaving the innermost atoms in a bulk-like environment. Again, the adequacy of the axial supercell size was checked by relaxing an 80-atom supercell and by noticing the small difference of 2 % between the inter-

face energies of the 60- and 80-atom supercells. The final interfacial configuration obtained with the two supercells showed no significant difference (smaller than 0.04 Å in all the atomic positions within the supercell)

B. Energetics and local atomic structure

The supercells for the metastable grain-boundary structures identified in the previous section were then fully relaxed with respect to the inter-granular separation (excess volume) and to all atomic positions. The interface energy was calculated as the difference between the total energy of the supercell, and the total energy of an equal number of Al_2O_3 formula units in the bulk phase, divided by the total grain-boundary area in the supercell.

1. $G(\text{Al})$ interface

First-principles LDFT calculations for the 60-atom supercell predict a small axial excess GB expansion (2% of a_{rho} , where $a_{\text{rho}}=5.086$ Å cf. Ref. 10) of the Al-terminated boundary, which lowers the interface energy from 1.92 J/m² (corresponding to 0% expansion) to 1.88 J/m² (for 2% expansion). This interface energy is a relatively high value, compared to the ones of the rhombohedral and basal twins, namely 0.63 J/m² (Ref. 10) and 0.73 J/m² (Ref. 11).

The local atomic environment of this interface, which we anticipate is the most ordered one among the three metastable structures considered in this study, is considerably more disordered than the ones at the rhombohedral or basal twins. For example the atomic arrangements on opposite sides of the GB are not equivalent (Figure 3). In terms of Al-O coordination, the cations in Al(1) are 5-fold coordinated while the ones in Al(1)* are 6-fold coordinated. The bond lengths are summarized in Table I and compared to the ones for bulk alumina.

In bulk alumina, each Al atom is coordinated by 6 anions at two characteristic distances of 1.84 and 1.96 Å. A similar splitting in the interfacial Al-O distances was observed in the most stable of the rhombohedral twin structures,¹¹ but not at the present $\Sigma 13$ twin interface, where the bond lengths of the shell of first neighbours are considerably more spread.

Similarly, there is a difference in coordination numbers between the oxygen atoms in O(2) and O(2)*, which are 4- and 3-fold coordinated respectively. All the other oxygen atoms are 4-fold coordinated. In particular, the atomic environment around the innermost O atom is well bulk-like with two bond lengths around 1.82 Å and two around 1.95 Å (cf. bulk values of 1.84 and 1.96 Å).

The effect of atomic relaxations at the interface, compared to the bulk volume, is described by the differences in interlayer spacings shown in Table II. The relaxation

involves mainly the first three atomic layers on both sides of the interface. As in the case of the bond lengths, there is a small difference between the atomic environment on opposite sides of the GB, which is also reflected in the change in interlayer distance (Table II). Note again that the central atoms are practically unaffected by the relaxations induced by the boundary. These results suggest that the boundary effects involve mainly a slab of ≈ 5 Å about the interface plane.

The free surface corresponding to this interface, denoted as FS(Al), was obtained by artificially forming two grains with Al-terminating surfaces. These can be described as obtained by cutting the bicrystal structure of Figure 3 between layers Al(1) and Al(1)* and by separating the grains until they do not interact any more. This is equivalent to consider only one of the two grains in the supercell and repeat it periodically along T_3 with a large lattice constant. The structure was then relaxed. The change in interlayer spacing due to relaxation is described in Table II. The outermost Al layer contracts inward, while the outermost O layer relaxes outward, so that the final surface configuration is O-terminated. The corresponding calculated surface energy is 2.77 J/m², a relatively high value compared to the ones of the basal surface (1.94 J/m² obtained by us with the present approach, which was also used for the basal twins in Ref. 11; 1.95 J/m² Ref. 35; 2.13 J/m² Ref. 36) and the rhombohedral surface (1.98 J/m² calculated with the present approach in Ref. 10).

2. $G(\text{O})$ interface

The axial relaxation of the G(O) interface, calculated by LDFT, yields that the minimum energy of 2.44 J/m² corresponds to an axial excess GB expansion of 6% of a_{rho} . The change in interlayer spacing due to atomic relaxation for the 60-atom cell is shown in Table II. It suggests that the relaxation involves a slab of ≈ 7 Å centered at the interface plane. In this case, the atomic environments on opposite sides of the boundary are equivalent. The boundary atoms O(0) are the most affected by the relaxation procedure, but also the inner O(2) and O(3) relax quite substantially (displacements of 4.6 % of a_{rho}).

The local atomic environment is summarized in Table I. Despite the large atomic relaxations, the interfacial oxygen O(0) are in a bulk-like environment, being 4-coordinated with two bond-lengths at 1.84 Å and two at 1.99 Å (cf. 1.84 Å and 1.96 Å in bulk). On the contrary, the next layers O(1) and O(2), and the inner layer O(4) are 3-fold coordinated. (The fourth bond from O(4), which points towards the interface, is elongated to 2.11 Å. This is the case also for the 80-atom cell. Hence, the 60-atom cell is appropriate.) Similarly, the first three cations layers Al(1), Al(2), and Al(3) are under-coordinated with only 5 oxygen neighbors. In the 80-atom supercell, the first atoms in bulk-like environ-

ment are the ones in Al(4), which are 6-fold coordinated, with three bond-lengths centered at 1.85 Å and three at 1.94 Å.

There are no obvious ways of defining a free surface from the interface configuration shown in Figure 5. One possible variant, that has the advantage of creating stoichiometric and equivalent surfaces, is to assign half of the interfacial atoms O(0) to one grain and half to the others. This creates a starting anion terminated configuration with a jagged structure. The structural minimization of this free surface leads to an oxygen terminated structure, indicated as FS(O), with a surface energy of 2.50 J/m², hence being more stable than FS(Al). The changes in interlayer spacing due to relaxation are included in Table II.

3. S(O) interface

We already discussed that the initially imposed translation state (0, 0.5) for this interface is not stable. Let us now specify this statement more precisely: the starting configuration (0, 0.5) identified with the shell-model calculations brings the oxygen atoms O(0) and O(1) very close together. We therefore started the LDFT structural optimization with a larger inter-granular distance T_3 (6 % of a_{rho}). The atomic relaxation increased the distance between the “close” O(0) and O(1) layers, and this induced also a change in the lateral translation state. The minimum energy of 2.71 J/m² is obtained at a rather large inter-granular separation, 12 % of a_{rho} , which produces a characteristic open boundary structure shown in Figure 6. In particular, there are large open channels along the boundary in the $[20\bar{2}1]$ direction, with a typical diameter of 6.7 Å. Here impurity or dopant atoms of different species could in principle be accommodated interstitially without involving severe elastic strains.

Atomic relaxations involve mainly the interfacial oxygen layer O(0) and the first three atomic layers on both sides. The changes in interlayer spacings are summarized in Table II. These results suggest that the boundary affects mainly a slab of ≈ 6 Å centered at the interface.

The innermost atoms Al(3) are practically unaffected by the interfacial relaxations, and thus they are in a bulk-like environment. The atomic distances of the first neighbouring O shell have the characteristic bulk-like splitting, three bond lengths being around 1.85 Å and three around 1.94 Å. On the interface, cations and anions are respectively 5-fold and 3-fold coordinated. However, the anions of the second layer O(2) have already the bulk coordination number of 4. The Al-O bond lengths are summarized in Table I.

The difference in interlayer separation between O(0)-O(1) and O(0)-O(1)*, respectively 1.6 and 0.78 Å (+8.5 % and -9.8 % of a_{rho} , respectively, cf. Table I), suggests the O(0)-O(1) plane as an alternative cleavage plane to the ones already mentioned. The two free surfaces obtained

by cleaving the bicrystal of Figure 6 at these planes are not stoichiometric and geometrically not equivalent, but the supercell is overall stoichiometric. Both these FS contribute to an average surface energy of 2.76 J/m². This average energy value provides some information about the possible cleavage mechanisms of alumina bicrystals, which we will discuss in the next section. Incidentally its value is close to the one of the surface energy of the stoichiometric Al-terminated surface (see section IV.B.1).

C. Large inter-granular separations: bonding and cleavage

Two sets of LDFT calculations monitored the interface energy as a function of large inter-granular separation in two different regimes. The starting points of the first one were the isolated grains with free surfaces, which were then brought closer, down to the formation of the three metastable interfaces previously described. These calculations are conceptually similar to the experimental procedure of diffusion bonding of bicrystals in ultrahigh vacuum, and should shed light on the boundary formation mechanisms. The starting points of the second set of calculations were the relaxed metastable translation states of the bicrystals, described in the previous section, which were then gradually pulled apart, up to the formation of the free surfaces. These calculations reveal insights into the cleavage mechanisms.

The fundamental difference between the two methods is that in the first case the cleavage plane is defined by an *a priori* choice of the free-surface terminating layer, while in the second case the cleavage plane is determined by the mechanical properties of the bicrystal, and therefore by the weakest bonds.

The LDFT results for the interface energies versus the axial component T_3 are shown in Figure 7. The energies corresponding to the first set of calculations (from free surfaces to internal boundaries) are connected with solid lines, while the values for the second set (from internal boundaries to free surfaces) are connected with dashed lines. Solid horizontal lines represent the limit of free surfaces, being twice the energy of the free stoichiometric surfaces FS(Al) and FS(O), 5.53 and 4.94 J/m² respectively. Each energy value corresponds to a fully relaxed configuration of atoms in the supercell.

Let us first concentrate on intergranular bonding, i.e., the formation of the two most stable structures, G(Al) and G(O), from the corresponding free stoichiometric surfaces FS(Al) and FS(O), by reducing the intergranular distance. Note that the relative energetic stability of the free surfaces is reversed with respect to that one of the bicrystals: FS(O) is more stable than FS(Al), and G(Al) is more stable than G(O). With decreasing distance, the interface energies remain close to the values of the corresponding free surfaces down to an intergranular distance of 2.54 Å (0.5 % of a_{rho}). There a significant difference

of more than 5 % appears due to the onset of interaction between the two slabs, and from there the values monotonically decrease down to the equilibrium metastable configurations G(Al) and G(O). The crossover point in the relative energetic stability, when the Al termination becomes more stable than the O termination, is around 1.8 Å (0.35 % of a_{rho}).

For intergranular cleavage, starting from the equilibrium interfaces G(Al) and G(O), and stretching the bicrystals along T_3 , the reverse energy paths as for the bonding procedure are followed up to displacements of 0.81 Å (0.16 % of a_{rho}). Subsequently, both the bicrystals react to the increase in intergranular distance by stretching the weakest bonds: the cleavage plane passes through O(1)*-O(2)* in G(Al) and through O(0)-O(1) in G(O). Cleavage on these planes create non-stoichiometric free surfaces, leaving two terminating oxygen atoms on one side and one on the other side.

At larger intergranular distances, the energies of the three metastable structures increase at the same rate, apparently to the same surface-energy limit. This may be understood by noticing that, in the limit of large separation, the two grains resulting from this ‘asymmetric’ cleavage in the G(Al) and G(O) supercells are structurally equal to the grains resulting from the cleavage through O(0)-O(1) in the S(O) supercell. Therefore, the corresponding three cleaved free surfaces become the same for large separation in the supercells. Their surface energies become equal to 2.26 J/m^2 , which is the average surface energy of the two non-stoichiometric terminating surfaces identified for S(O) (see section IV.B.3).

D. Electronic structure

The self-consistent LDFT results obtained for the three equilibrium metastable interface configurations were used to investigate the effect of the interfacial local atomic arrangements on the electronic structures of alumina bicrystals. In particular, we focus on the site-projected density of states (PDOS). We define the PDOS as the projection of the total density of states (DOS) on partial waves inside spheres centered on atomic sites. The radius of the spheres were 1.27 Å and 0.58 Å for oxygen and aluminium sites, respectively. The crystal Bloch eigenstates were calculated on a $6 \times 6 \times 2$ \mathbf{k} -point mesh and broadened with Gaussians of 0.8 eV width. The same setup was used in the analysis of the rhombohedral $\Sigma 7$ and basal $\Sigma 3$ twin boundaries.^{10,11}

The results are shown in Figure 8, where the oxygen-PDOS (O-PDOS) of the three interface states are compared with the O-PDOS of bulk alumina. The latter is indicated by a thick solid line, while a dashed line and a thin solid line indicate the PDOS of oxygen atoms, close and far from the interface, respectively. To facilitate the discussion of the results, the interfaces PDOS have been rigidly shifted so that the bulk-like O-PDOS (thin solid

lines) is on top of the O-PDOS for bulk alumina (thick solid line). The zero of energy in the plot is the Fermi level of the bulk supercell (the energy eigenvalue of the highest occupied valence state), and the Fermi levels of the supercells containing the interfaces are marked with vertical solid lines.

A discussion of the Al-PDOS is not given here because, as already considered in Ref. 10, it is less illustrative than the O-PDOS in $\alpha\text{-Al}_2\text{O}_3$: Due to the high ionic character of the Al-O bond in alumina, all the features of the DOS (up to ≈ 20 eV) are dominated by the O-PDOS, the contribution of the Al-PDOS being 5–10 times smaller, and similar in the spectral shape of peaks and shoulders, even in the lower conduction band region.

Let us first emphasize the similarity between the O-PDOS in bulk alumina (thick solid lines) with the ones in bulk-like environment far from the interfaces (thin solid lines). There are hardly any differences in the lower valence band (with energies centered around -17 eV), and minor differences in the higher valence band (with energies centered around -5 eV) and in the conduction band. This shows that the effect of the local environment on the electronic structure is localized within the first 2-3 interfacial oxygen layers, the most affected being always the interfacial ions (dashed lines), as intuitively expected and already observed at the rhombohedral $\Sigma 7$ twin boundary in Ref. 10. This further confirms that the supercell dimension along T_3 is sufficiently large to leave the inner atoms in a bulk-like environment.

We now discuss the differences between the interfacial and bulk-like valence O-PDOS. Let us first notice that the $\Sigma 13$ GB affect both the lower and higher valence bands of the interfacial O atoms. The differences are moderate in G(Al), where the interfacial O-PDOS corresponding to O(1) and O(1)* (dashed lines in Figure 8a), have still the characteristic bulk-like structure (thin solid line). The biggest deviation appears for O(1)*, which is 5-fold coordinated. More pronounced differences are present in G(O), where the interfacial O-PDOS (O(0) and O(1)=O(1)*, dashed lines in Figure 8b) are qualitatively different from the bulk-like structure (thin solid line): the states corresponding to O(1) (3-fold coordinated) are redistributed towards higher energies, while the states corresponding to the O(0) (4-fold coordinated) higher valence bands are redistributed towards lower energies, forming a two-peak structure. The high-energy S(O) boundary induces considerably more drastic changes in the electronic structure. The lower valence band is rigidly shifted by 1.8 eV to higher energies, and a three-peak spectral shape appears in the higher band. Let us also note that the valence-band edges for the G(Al), G(O), and S(O) supercells, respectively, are 0.2 eV, 0.9 eV, and 1.3 eV higher than for bulk alumina.

The changes in the unoccupied region of the O-PDOS are now addressed. The main feature, common to the three interfaces, is the presence of a pre-peak in the energy gap, at 6-7 eV, just below the conduction-band edge. A similar gap state was observed in the highest energy

structure of the rhombohedral twin. The fundamental band gap of bulk alumina (6.6 eV with the LDFT method used in the present calculations) is therefore reduced by the presence of this pre-peak to 5.41 eV in G(Al), 4.47 eV in G(O) and 3.72 eV in S(O).

The real-space projection along $[1\bar{2}10]$ of the density of unoccupied electron states in the energy range between 5 and 7 eV is shown in Figure 9 for the G(Al) interface, taken as the representative case. The density is proportional to the grey-scale, ranging from white for zero density, to black for the highest density. The projected atomic positions in the supercell are marked by the labels Al and O. Note that most density of the electron states corresponding to the pre-peak is spatially confined at the interface, and that a considerable density fraction is localized on the first three interfacial O atoms.

At higher energies, between 10 and 20 eV, the three interfaces modify the interfacial O-PDOS substantially with respect to the bulk three-peak signal. Moreover, within the same boundary structure, there are significant differences between the O-PDOS corresponding to different interfacial sites, like O(1) and O(1)* in G(Al), or O(0) and O(1) in G(O). This is likely to play an important role in the interpretation of experimental ELNES spectra (cf, e.g. Ref 13).

As demonstrated in Ref. 13 for the rhombohedral $\Sigma 7$ twin boundary, the ELNES of the oxygen core-level ionisation K edge, which is approximately proportional to the conduction band PDOS of angular-momentum p character at oxygen sites, can provide experimental informations to distinguish the local electronic states and atomic coordination at oxygen sites located in the bulk volume or at interfaces. The calculated O-PDOS for the unoccupied conduction-band states of the $\Sigma 13$ twin boundary indicate characteristic differences between the three metastable structural models obtained by the LDFT structure optimisation. Hence, an ELNES experiment with a $\Sigma 13$ twin bicrystal in a scanning transmission electron microscope with sufficiently high spatial and energetic resolutions, comparably to the ELNES experiment of Ref. 13, appears very promising to augment our theoretical characterisation of this interface.

V. CONCLUSIONS

The energetic, structural, and electronic properties of the $\Sigma 13$ ($10\bar{1}4$) mirror twin boundary in α -Al₂O₃ were studied by atomistic modelling with both empirical shell-model potentials and first-principles LDFT calculations. Three metastable variants of the interface were identified, one Al-terminated boundary, G(Al), and two O-terminated boundaries, G(O) and S(O). The lowest-energy interface is Al-terminated, as previously predicted by empirical shell-model potentials.^{23,22} The interfacial energies of the fully relaxed interfaces, as calculated with LDFT, were discussed.

Despite the thermodynamic stability of the G(Al) interface over the O-terminating variants, a high-resolution transmission electron microscopy (HRTEM) experiment with high-purity diffusion-bonded bicrystals detected the G(O) boundary, rather than the G(Al) one.²² In order to clarify these observations, the formation of the G(Al) and G(O) boundaries was studied by gradually reducing the intergranular distance, starting from the corresponding free surfaces FS(Al) and FS(O), to model theoretically the procedure of diffusive bonding in ultrahigh vacuum. This showed that the relative energetic stability between these two interfaces depends on the intergranular separation, and is actually reversed for the free surfaces, FS(O) being more stable than FS(Al). From this a possible explanation for the HRTEM observations emerges: prior to bonding the free surfaces are O-terminated. When the crystals are diffusion bonded, the equilibrium thermodynamics would drive the atomic reconstruction of the O-terminated interface into the Al-terminated one, G(Al). However, the energy barrier for such a reconstructive transformation is apparently too high, as long as no additional Al is provided in the bonding process, and the bicrystal is therefore locked in the metastable G(O) configuration.

The analysis of the site-projected densities of states showed that the effect of the interfaces on the electronic structure is localized within 5-7 Å around the boundary plane, and affects mostly the upper valence band and the conduction bands. In particular, the three variants of the $\Sigma 13$ boundary narrow the band gap by defect states below the conduction-band edge, which are highly localized at the interface.

An important final conclusion of this work is that, although the $\Sigma 13$ twin boundary has a short lateral periodicity (which enables the thorough treatment by LDFT), the resulting structural complexities, as well as the interface energies of its metastable configurations, are significantly higher than those of the previously investigated rhombohedral $\Sigma 7$ and basal $\Sigma 3$ twin boundaries, usually called “special” grain boundaries. The $\Sigma 13$ interface is therefore a promising model case for “general” grain boundaries in α -Al₂O₃. We anticipate that it will be useful to provide a theoretical understanding of the influence of segregated cation impurities on the structure and energetics of alumina interfaces.

ACKNOWLEDGMENTS

This project was financially supported by the Deutsche Forschungsgemeinschaft (project El 155/4-1). The authors thank A. G. Marinopoulos for his help in the beginning of the work, S. Nufer for valuable communications concerning ELNES experiment and theory, T. Höche, M. W. Finnis and M. Rühle for helpful discussions.

TABLE I. Equilibrium Al-O distances in the interfacial and bulk-like regions of the G(Al), G(O), and S(O) supercells. For comparison, there are two Al-O distances in bulk α -Al₂O₃, with calculated values of 1.84 Å and 1.96 Å.

GB region			bulk-like region		
<i>G(Al)</i>			<i>G(O)</i>		
Al(1)*-O		Al(1)-O	Al(1)-O	O(5)-Al	
1.82 1.90 1.93		1.81 1.82	1.80 1.85		
1.94 1.96 2.00		1.93 1.95 2.00	1.94 1.97		
<i>G(O)</i>			<i>S(O)</i>		
O(1)*-Al	O(0)-Al	O(1)-Al	Al(3)-O		
1.77 1.80	1.84 (2x)	1.77 1.80	1.83 1.84 1.87		
1.92	1.99 (2x)	1.92	1.93 1.95 1.97		
O(1)*-Al	O(0)-Al	O(1)-Al	Al(3)-O		
1.81 1.88	1.77 1.77	1.76 1.81	1.84 1.84 1.89		
1.93	1.81	2.01	1.93 1.94 1.97		

TABLE II. LDFT results for interface energies, axial expansions along T_3 (in % of a_{rho}) and changes in interlayer spacings (in % of a_{rho}) for the structurally relaxed twin interfaces and free surfaces.

	G(Al) FS(Al)		G(O) S(O) FS(O)			
E_{int} (J/m ²)	1.88	2.77	E_{int} (J/m ²)	2.44	2.71	2.47
T_3	2	-	T_3	6	12	-
Al(3)*-O(4)*	0.2	0.5	O(4)*-Al(3)*	-0.5	-0.5	-1.5
Al(2)*-Al(3)*	-0.3	0.7	O(3)*-O(4)*	0.6	-0.3	1.5
O(3)*-Al(2)*	-1.1	1.9	O(2)*-O(3)*	4.6	0.6	0.9
O(2)*-O(3)*	-2.5	-3.0	Al(2)*-O(2)*	-2.2	1.1	-3.8
O(1)*-O(2)*	2.1	10.1	Al(1)*-Al(2)*	-3.9	-0.4	-0.8
Al(1)*-O(1)*	0	-11.0	O(1)*-Al(1)*	-2.8	1.3	3.8
			O(0)-O(1)*	7.3	-9.8	0.6
Al(1)*-Al(1)	1.7	∞	O(0)-O(1)	7.3	8.5	0.6
Al(1)-O(1)	3.0	-11.0	O(1)-Al(1)	-2.8	-3	3.8
O(1)-O(2)	-6.1	10.1	Al(1)-Al(2)	-3.9	5.6	-0.8
O(2)-O(3)	3.0	-3.0	Al(2)-O(2)	-2.2	-2.9	-3.8
O(3)-Al(2)	0.4	1.9	O(2)-O(3)	4.6	-2.5	0.9
Al(2)-Al(3)	-1.4	0.7	O(3)-O(4)	0.6	3.5	1.5
Al(3)-O(4)	0.6	0.5	O(4)-Al(3)	-0.5	-0.1	-1.5

FIG. 1. Corundum structure of α -Al₂O₃ viewed from the $[1\bar{2}10]$ direction. Oxygen and aluminium atoms are represented by light-gray and black circles, respectively. Dashed lines mark the $(10\bar{1}4)$ planes leading to stoichiometric $\Sigma 13$ interfaces with Al (B) and O (C) terminations, respectively.

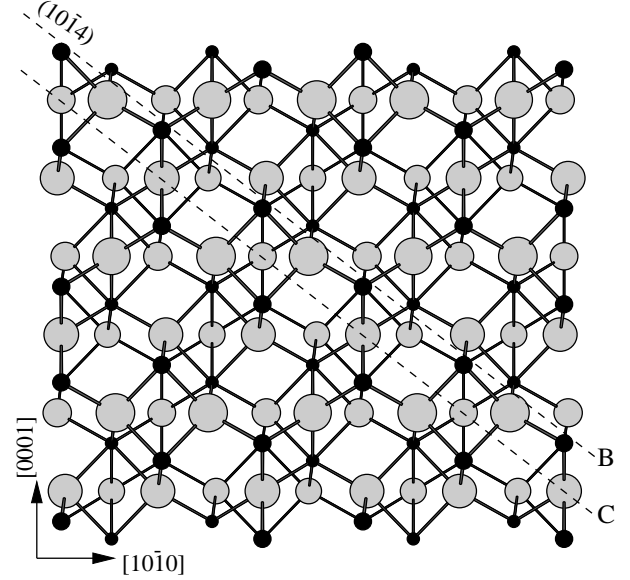


FIG. 2. Shell-model total energy (Ry/supercell) for the cation terminated interfaces as a function of the lateral translation state $T_1\mathbf{e}_1 + T_2\mathbf{e}_2$, with $\mathbf{e}_1=[20\bar{2}\bar{1}]$ and $\mathbf{e}_2=[1\bar{2}10]$.

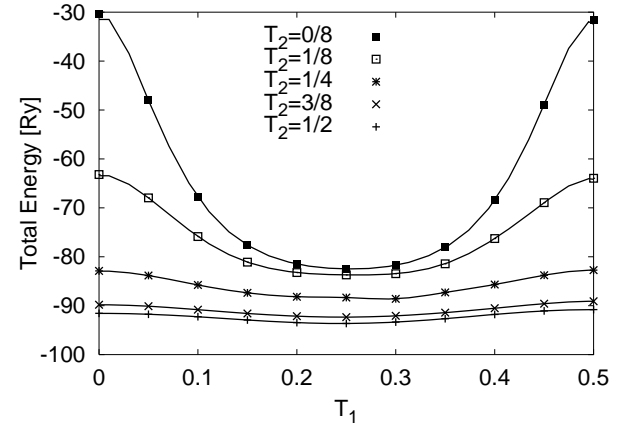


FIG. 3. LDFT result for the relaxed atomic structure of the G(Al) interface viewed along the $[1\bar{2}10]$ direction. The atoms are represented as in Figure 1, and the labels on the right-hand side identify the atomic layers. The dashed box indicates the axial size of the 60-atom supercell in the $[50\bar{5}4]$ direction, and both the size and lateral translation-state in the $[20\bar{2}\bar{1}]$ direction. The supercell contains two equivalent horizontal interfaces, one in the middle (marked by the dotted line), and one both at the top and bottom ends (marked by the dashed line segments) arising from the periodic boundary conditions in the $[50\bar{5}4]$ direction.

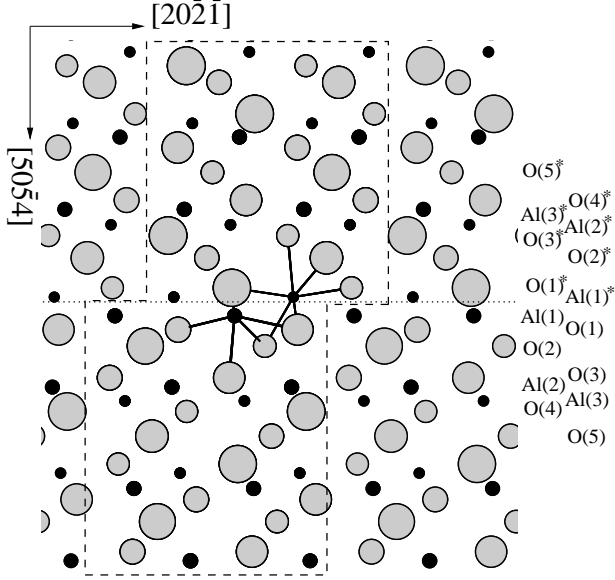


FIG. 4. Shell-model total energy for the anion terminated interfaces as a function of the lateral translation state $T_1\mathbf{e}_1 + T_2\mathbf{e}_2$, where $\mathbf{e}_1=[20\bar{2}\bar{1}]$ and $\mathbf{e}_2=[1\bar{2}10]$.

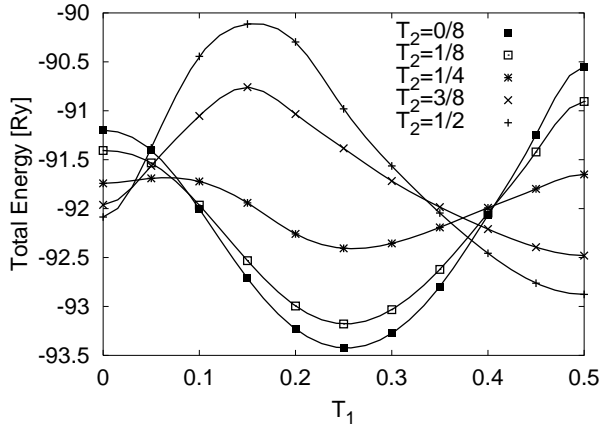


FIG. 5. LDFT result for the relaxed atomic structure of the G(O) interface viewed along the $[1\bar{2}10]$ direction. Atoms, labels, and symbols as in Figure 3.

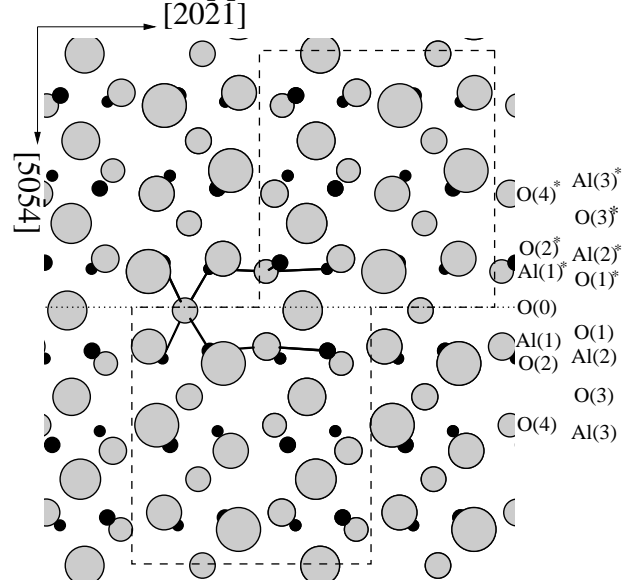


FIG. 6. LDFT result for the relaxed atomic structure of the S(O) interface viewed along the $[1\bar{2}10]$ direction. Atoms, labels, and symbols as in Figure 3.

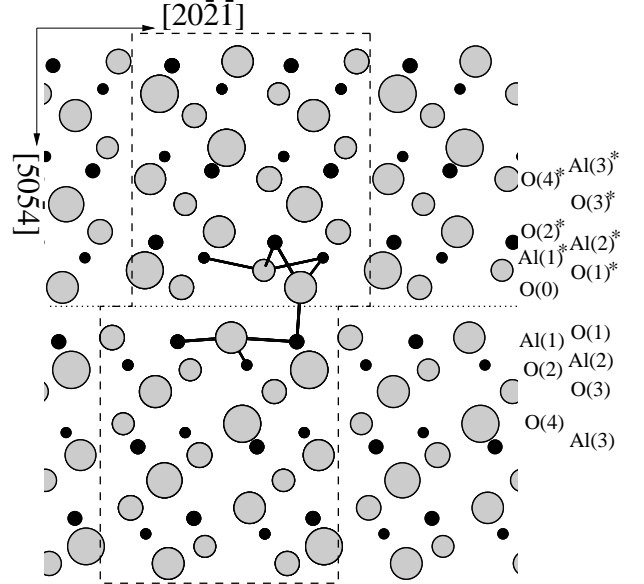


FIG. 7. Interface energies (in J/m^2) versus the axial intergranular separation (in % of a_{rtho}) for the three metastable interfaces G(Al), G(O), and S(O). The solid (dashed) lines connect the results obtained by reducing (increasing) the intergranular separation from free surfaces (internal interfaces) down to the the formation of the internal boundaries (free surfaces). Solid horizontal lines represent twice the energies of the free surfaces FS(Al) and FS(O) (cf. Table II; NB: upon interfacial separation the interface energy goes to twice the surface energy because the resulting surface area is twice the initial interface area).

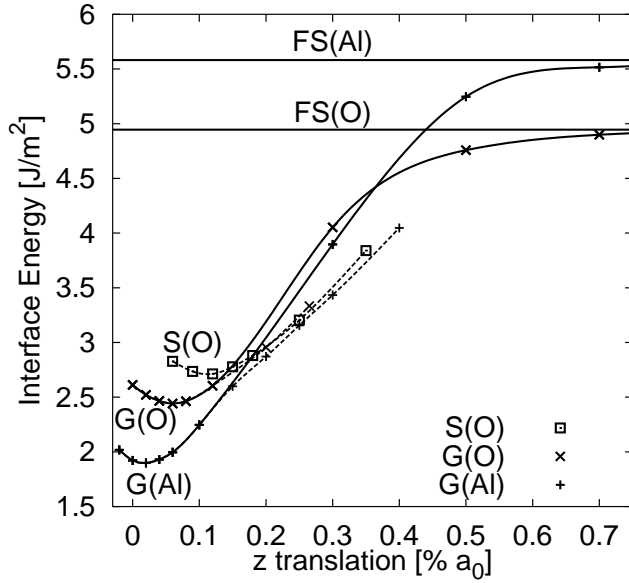


FIG. 8. a) O-PDOS for the G(Al), b) for the G(O), and c) for the S(O) interfaces. The zero of energy is the Fermi level (energy eigenvalue of the highest occupied valence-band state) of the bulk supercell, the interfaces PDOS have been rigidly shifted so that the bulk-like O-PDOS (thin solid lines) is on top of the O-PDOS for bulk alumina (thick solid line). The Fermi levels of the supercells containing the interfaces are marked by solid vertical lines.

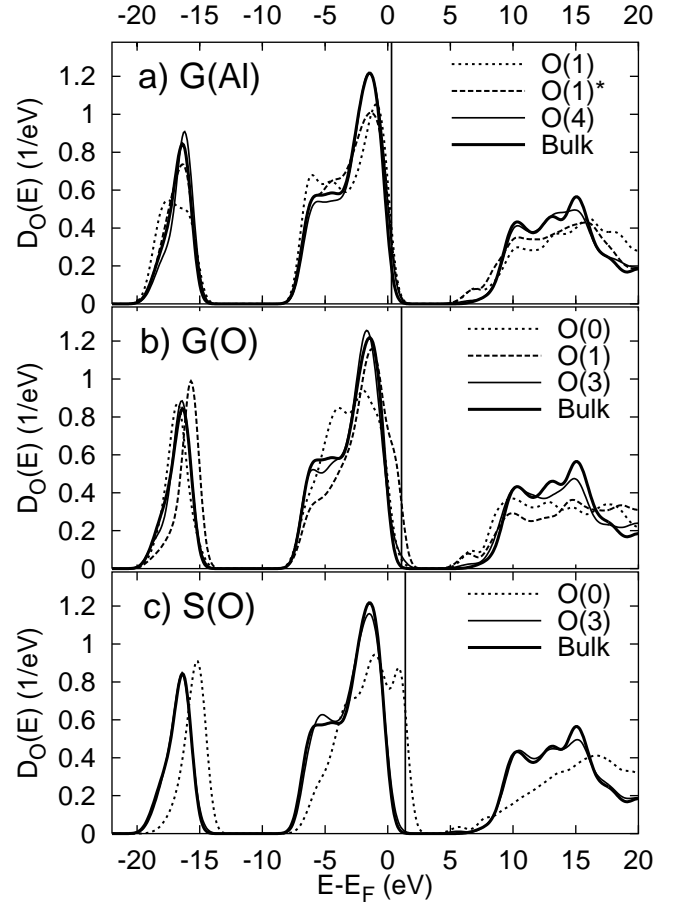
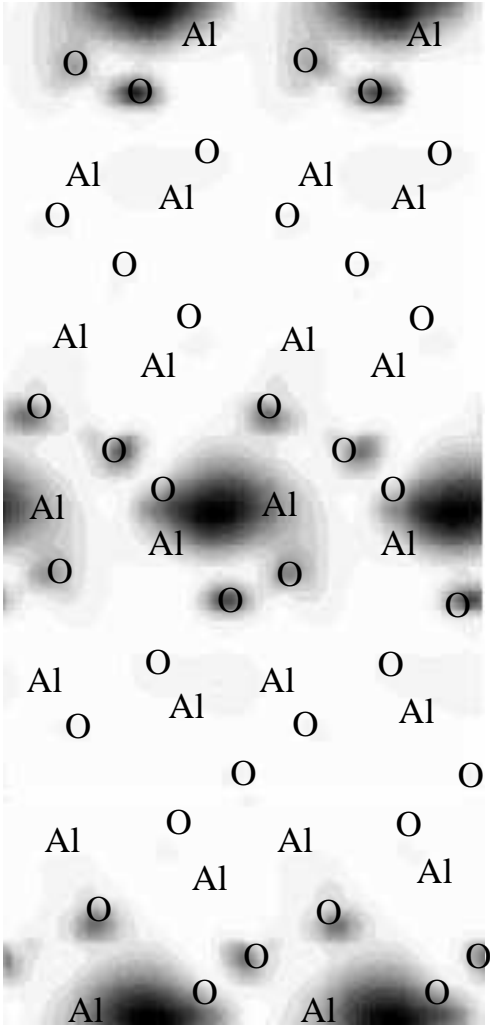


FIG. 9. Real-space projection along the $[1\bar{2}10]$ direction of the density distribution of unoccupied electron states in the energy range between 5 and 7 eV for the G(Al) interface. Al and O labels mark the projected atomic positions in the supercell.



¹ *Structure and Properties of MgO and Al₂O₃ Ceramics*, Vol. 10 of *Advances in Ceramics*, edited by W. D. Kingery (The American Ceramic Society, Columbus, Ohio, 1984).

² J. Cawley and J. W. Halloran, *J. Am. Ceram. Soc.* **69**, 195 (1986).

³ S. I. Bae and S. Baik, *J. Am. Ceram. Soc.* **76**, 1065 (1993).

⁴ C.-W. Li and W. D. Kingery, in *Structure and Properties of MgO and Al₂O₃ Ceramics*, Vol. 10 of *Advances in Ceramics*, The American Ceramic Society, edited by W. D. Kingery (The American Ceramic Society, Columbus, Ohio, 1984), p. 368.

⁵ S. Lartigue, L. Priester, F. Dupau, P. Gruffel, and C. Carry, *Mater. Sci. Eng.* **A164**, 211 (1993).

- ⁶ J. Cho, M. P. Harmer, H. M. Chan, J. M. Rickman, and A. M. Thompson, *J. Am. Ceram. Soc.* **80**, 1013 (1997).
- ⁷ S. I. Bae and S. Baik, *J. Mater. Sci.* **28**, 4197 (1993).
- ⁸ A. W. Funkenbusch and D. W. Smith, *Metall. Trans.* **6A**, 2299 (1975).
- ⁹ R. S. Jupp, D. F. Stein, and D. W. Smith, *J. Mater. Sci.* **15**, 96 (1980).
- ¹⁰ A. G. Marinopoulos and C. Elsässer, *Acta Mater.* **48**, 4375 (2000).
- ¹¹ A. G. Marinopoulos, S. Nufer, and C. Elsässer, *Phys. Rev. B* **63**, 165112 (2001).
- ¹² C. Elsässer and A. G. Marinopoulos, *Acta Mater.* accepted for publication (2001).
- ¹³ S. Nufer, A. G. Marinopoulos, T. Gemming, C. Elsässer, W. Kurtz, S. Köstlmeier, and M. Rühle, *Phys. Rev. Lett.* **86**, 5066 (2001).
- ¹⁴ S. Fabris, S. Nufer, and C. Elsässer, in preparation.
- ¹⁵ D. Bouchet, F. Dupau, and S. Lartigue-Korinek, *Microsc. Microanal. Microstrut.* **4**, 561 (1993).
- ¹⁶ W. Swiatnicki, S. Lartigue-Korinek, and J. Laval, *Acta Metall. Mater.* **43**, 795 (1995).
- ¹⁷ C. Kittel, *Solid State Physics* (John Wiley and Sons, Inc., New York, 1976).
- ¹⁸ S. Nufer, doctoral thesis, Universität Stuttgart, in preparation.
- ¹⁹ W. D. Kaplan, H. Müllejans, M. Rühle, J. Rodel, and N. Claussen, *J. Am. Ceram. Soc.* **78**, 2841 (1995).
- ²⁰ R. Brydson, S. C. Chen, F. L. Riley, S. J. Milne, X. Q. Pan, and M. Rühle, *J. Am. Ceram. Soc.* **81**, 369 (1998).
- ²¹ T. Höche and M. Rühle, *J. Am. Ceram. Soc.* **79**, 1961 (1996).
- ²² T. Höche, P. R. Kenway, H.-J. Kleebe, M. W. Finnis, and M. Rühle, *J. Phys. Chem. Solids* **55**, 1067 (1994).
- ²³ P. R. Kenway, *J. Am. Ceram. Soc.* **77**, 349 (1994).
- ²⁴ M. Exner and M. W. Finnis, *Material Science Forum* **207-209**, 225 (1996).
- ²⁵ Y.-M. Huang, M. Exner, M. Wilson, and M. W. Finnis (unpublished).
- ²⁶ T. Höche, doctoral thesis, Universität Stuttgart, 1994.
- ²⁷ A. G. Marinopoulos and C. Elsässer, *Phil. Mag. Lett.* **81**, 329 (2001).
- ²⁸ G. V. Lewis and C. R. A. Catlow, *J. Phys. C* **18**, 1149 (1985).
- ²⁹ C. Elsässer, N. Takeuchi, K. M. Ho, C. T. Chan, P. Braun, and M. Fähnle, *J. Phys. C* **2**, 4371 (1990).
- ³⁰ K. M. Ho, C. Elsässer, C. T. Chan, and M. Fähnle, *J. Phys.: Condens. Matter* **4**, 5189 (1992).
- ³¹ C. Elsässer, doctoral thesis, Universität Stuttgart, 1990.
- ³² B. Meyer, doctoral thesis, Universität Stuttgart, 1998.
- ³³ B. Meyer, C. Elsässer, and M. Fähnle, Fortran 90 Program for Mixed-Basis Pseudopotential Calculations for Crystals, Max-Planck-Institut für Metallforschung Stuttgart (unpublished).
- ³⁴ J. D. Gale, *J. Chem. Soc. - Faraday Transact.* **93**, 629 (1997).
- ³⁵ I. Batirev, A. Alavi, M. W. Finnis, and T. Deutsch, *Phys. Rev. Lett.* **82**, 1510 (1999).
- ³⁶ X.-G. Wang, A. Chaka, and M. Scheffler, *Phys. Rev. Lett.* **84**, 3650 (2000).